

# Ion and Electron Acoustic Bursts during Anti-Parallel Reconnection Driven by Lasers

S. Zhang, A. Chien, L. Gao, H. Ji, E. Blackman, R. Follett, D. Froula, J. Moody, H. Chen

March 15, 2022

**Nature Physics** 

#### Disclaimer

This document was prepared as an account of work sponsored by an agency of the United States government. Neither the United States government nor Lawrence Livermore National Security, LLC, nor any of their employees makes any warranty, expressed or implied, or assumes any legal liability or responsibility for the accuracy, completeness, or usefulness of any information, apparatus, product, or process disclosed, or represents that its use would not infringe privately owned rights. Reference herein to any specific commercial product, process, or service by trade name, trademark, manufacturer, or otherwise does not necessarily constitute or imply its endorsement, recommendation, or favoring by the United States government or Lawrence Livermore National Security, LLC. The views and opinions of authors expressed herein do not necessarily state or reflect those of the United States government or Lawrence Livermore National Security, LLC, and shall not be used for advertising or product endorsement purposes.

### Ion and Electron Acoustic Bursts during Anti-Parallel Reconnection Driven by Lasers

Shu Zhang,<sup>1,\*</sup> Abraham Chien,<sup>1</sup> Lan Gao,<sup>2</sup> Hantao Ji,<sup>1,2,†</sup> Eric G. Blackman,<sup>3</sup> Russ Follett,<sup>4</sup> Dustin H. Froula,<sup>4</sup> Joseph Katz,<sup>4</sup> William Daughton,<sup>5</sup> Chikang Li,<sup>6</sup> Andrew Birkel,<sup>6</sup> Richard Petrasso,<sup>6</sup> John Moody,<sup>7</sup> and Hui Chen<sup>7</sup>

<sup>1</sup>Department of Astrophysical Sciences, Princeton University, Princeton, New Jersey 08544, USA

<sup>2</sup>Princeton Plasma Physics Laboratory, Princeton University, Princeton, New Jersey 08543, USA

<sup>3</sup>Department of Physics and Astronomy, University of Rochester, Rochester, New York 14627, USA

<sup>4</sup>Laboratory for Laser Energetics, University of Rochester, Rochester, New York 14623, USA

<sup>5</sup>Los Alamos National Laboratory, Los Alamos, New Mexico 87545, USA

<sup>6</sup>Plasma Science and Fusion Center, Massachusetts Institute of Technology, Cambridge, Massachusetts 02139, USA

<sup>7</sup>Lawrence Livermore National Laboratory, Livermore, California 94550, USA

(Dated: February 18, 2022)

Magnetic reconnection is ubiquitous in space and astrophysical plasmas rapidly converting magnetic field energy into plasma particles. Among numerous candidate kinetic mechanisms, ion acoustic instabilities driven by the relative drift between ions and electrons, or electric current, have been long hypothesized to play a critical role in dissipating magnetic energy in collisionless plasmas, but their effectiveness and even existence during reconnection remain elusive due to ion Landau damping and difficulties in detecting on the Debye length scale in the laboratory. Here we report a clear identification of sudden onset of ion acoustic bursts by collective Thomson scattering diagnostics in the exhaust of anti-parallel reconnection magnetically driven in high-Z plasmas at low beta on a novel platform using high-power lasers. The ion acoustic bursts are followed by electron acoustic bursts with electron heating and bulk acceleration. These observations are successfully reproduced by 1D and 2D Particle-in-Cell simulations in which ion acoustic instabilities, driven by current due to electron jet in the reconnection exhaust, grow rapidly to form electrostatic double layers. These double layers in turn induce electron two-stream instability to generate electron acoustic bursts, during which electrons are heated and accelerated in accordance with the measurements. Our results demonstrate the importance of ion and electron acoustic dynamics during magnetic reconnection when ion Landau damping is ineffective, a condition that may exist in many plasmas including near-Earth space, stellar flares, and black hole accretion engines.

Magnetic reconnection is a fundamental physical process through which energy is rapidly converted from magnetic field to plasma by alternating magnetic topology [1, 2]. It has been a longstanding challenge to identify the underlying kinetic mechanisms for efficient dissipation required for the topological change as well as energy conversion to explain the observed fast reconnection in nearly collisionless plasmas in space and astrophysics. There has been progress in understanding and confirming 2D kinetic mechanisms often represented by nongyrotropic pressure tensor [3–6] in the electron diffusion regions (EDRs) where field lines break and reconnect. Beyond these 2D laminar processes, however, the kinetic dissipation mechanisms operating in general 3D are still much less understood [7, 8] within or near diffusion regions and separatrices [9] that feature strong spatial gradients and streaming. They include various plasma waves or instabilities, such as whistler waves [10, 11], Buneman instabilities [12–14], lower-hybrid drift waves (LHDW) [15–22] (due to cross-field gradient [23] or cross-field drift [24]), drift kink [25] or kinetic Kelvin-Helmholtz [26] instabilities.

Among these 3D candidate dissipation mechanisms, unstable ion-acoustic waves (IAWs) [27–30] driven by relative drift between electrons and ions, or equivalently electric current, have attracted considerable interest as potential sources for the enhanced resistivity or viscos-

ity that is often used within fluid descriptions as a local, current-dependent anomalous resistivity required for the sustained Petschek model of fast reconnection [31–36]. Despite early pioneering laboratory detection [37], however, the importance of IAWs for magnetic reconnection has been quickly dismissed due to the widely observed high ion temperature  $(T_i/Z \gtrsim T_e)$  in space and in the laboratory where IAWs are strongly stabilized by ion Landau dumping. Technical difficulties in the laboratory in measuring plasma waves in the short wavelengths on the order of Debye length have also prevented progress on identifying IAWs and understanding their detailed properties and role in magnetic reconnection.

In this Article, we present a novel laboratory platform where reconnection is driven magnetically at low- $\beta$  by laser-powered capacitor coils [38] in high-Z plasmas where  $T_i/Z \ll T_e$ . Sudden onset of bursts of IAWs is successfully measured for the first time in the exhaust region by collective Thomson scattering diagnostics. The IAWs are followed by bursts of electron acoustic waves (EAWs) with electron heating and bulk acceleration. The corresponding Particle-in-Cell (PIC) simulations in 1D and 2D show that IAWs are destabilized by electron exhaust jet where relative drift between ions and electrons are large. IAWs grow rapidly to form electrostatic double layers which in turn accelerate electrons to drive two-stream instability generating bursts of EAWs while heat-

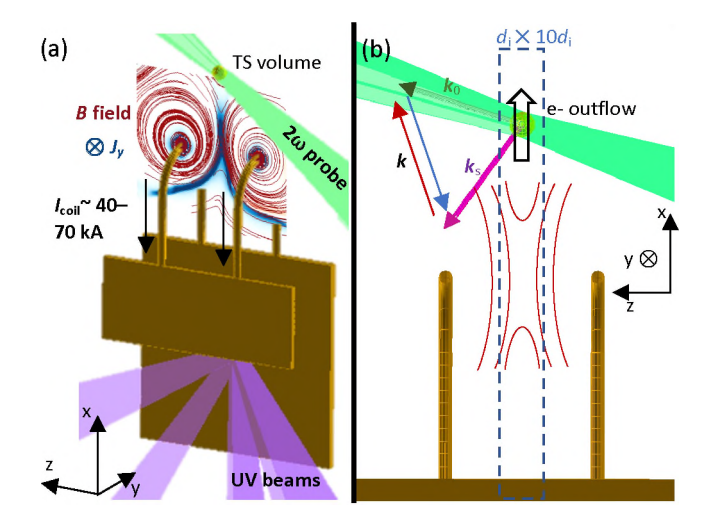


FIG. 1. Experimental setup. Six UV beams are used to irradiate the back plate of the capacitor, driving current in the coils with  $I_{\rm coil} \sim 40-70$  kA. FLASH MHD simulation results are overlapped in (a) to show the structure of the magnetic field (red lines) and the out-of-plane current density (blue) in the y-direction. A  $2\omega$  (527 nm) Thomson scattering beam (green) probes the reconnection exhaust region, 600 μm above the center point between the top of the coils. The scattered light in a volume  $60 \times 60 \times 50 \text{ }\mu\text{m}^3$  is collected by an f/10 reflective collection system.  $\mathbf{k}_0$  and  $\mathbf{k}_s$  in (b) are the wavevectors of the probe beam and the collected scattered light. The red and blue arrows indicate wavevectors (k) of waves in plasma resonant with the probe and the scattered light. The red arrow is for the wave generating redshifted scattered light, and the blue arrow is for the wave generating blueshifted scattered light. These k's are in the x-y plane and  $17^{\circ}$ off the outflow direction. The blue dashed box indicates a  $d_i \times 10d_i = 180 \ \mu \text{m} \times 1800 \ \mu \text{m}$  region, in which  $d_i = c/\omega_{\text{pi}}$ .

ing electrons. Our results demonstrate the importance of ion and electron acoustic dynamics causing bursty energy dissipation during magnetic reconnection when ion Landau damping is ineffective. Implications for reconnection process in magnetically dominated plasmas during stellar flares and accretion onto black holes are discussed.

## RECONNECTION PLATFORM WITH LASER-DRIVEN CAPACITOR COILS

The presented experiments were performed on the OMEGA laser facility at the Laboratory for Laser Energetics, University of Rochester [39]. The experimental platform is shown in Fig. 1. The capacitor-coil target is made of a 50  $\mu m$  thick Cu foil. The coils have a 600  $\mu m$  diameter and 500- $\mu m$ -length legs, and are separated by 600  $\mu m$ . Six beams of 500 J 1-ns UV ( $\lambda=351~nm$ ) lasers are focused on the center of the capacitor's backplate to drive a  $\sim 40-70~kA$  current in the coils. A reconnection current sheet can be formed between the capacitor coils.

The magnetic field generated by the capacitor-coil tar-

gets is measured by using proton radiography [40–42]. The upstream magnetic field strength is  $\sim 23-40$  T at 6 ns after the lasers' onset. The proton radiographs also show the center feature indicating the reconnection current sheet [41]. To further quantify the reconnection conditions, we have conducted radiative and nonideal magnetohydrodynamic (rad-MHD) simulations using the FLASH code [43] to simulate plasma diffusing from the capacitor plates and the plasma emerging from the heated coils due to Ohmic heating and x-ray radiation. The supplemental materials detail the setup of the non-ideal rad-MHD simulation. The simulated magnetic field lines and the current density at 3 ns, overlapped on the target in Fig. 1(a), show that a reconnection current sheet is formed between the coils. This reconnection current sheet lasts until 10 ns, as shown in Fig. S2. The synthetic proton radiographs shown in Fig. S3 have a central flask-like feature due to the current sheet, consistent with the experimental one.

The Thomson scattering probe laser ( $\lambda=527$  nm, 150 J energy, 3.7 ns square pulse, 60 µm spot size) is focused at 600 µm above the center between the top of the coils as shown in Fig. 1. In this experiment, due to the low density ( $n_{\rm e}\sim5\times10^{18}~{\rm cm}^{-3}$ ) in the scattering volume, the electron density fluctuations scattering the light have  $k\sim k_0=2\pi/527~{\rm nm}^{-1}$  in the direction 17° from the outflow direction (+ $\boldsymbol{x}$ ) shown as the  $\boldsymbol{k}$ 's in Fig.1(b).

## BURSTS OF ION AND ELECTRON ACOUSTIC WAVES AND ELECTRON HEATING

The Thomson scattering from the ion-acoustic waves (IAW) reveals that current-driven instabilities develop at 7 ns. The narrowband spectrometer captured the asymmetric (10:1) IAW-resonant peaks which grow from thermal level by three orders of magnitude to extremely asymmetric ( $\sim 100:1$ ), intense, and bursty IAW peaks during 7-8 ns. This is shown in Fig. 2(a), as a sign of the ion turbulence induced by unstable IAW [44]. The asymmetry in the IAW Stokes and anti-Stokes peaks is due to the electrons drifting relative to ions. As shown in Fig. 2c, the Thomson scattering spectrum lineout before the IAW bursts (along the dashed line in Fig. 2a) can be reproduced in the synthetic spectrum (green dashed line in Fig. 2c) when electrons ( $n_e = 5 \times 10^{18} \text{ cm}^{-3}$ ,  $T_e =$ 200 eV) are drifting with  $v_{\rm d} = 0.17 \sqrt{T_{\rm e}/m_{\rm e}}$  relative to ions ( $T_i = 400 \text{ eV}, Z = 18$ ). The IAW-resonant peak is broader than the synthetic spectrum (green dashed line) without considering the inhomogeneous flow velocity, but can be reproduced by including an inhomogeneous flow velocity in the scattering volume with  $\Delta v = 2 \times 10^4$  m/s. The synthetic spectrum is calculated assuming the resonant wave is stable and the density fluctuations are in thermal level. However, based on the electrostatic dis-

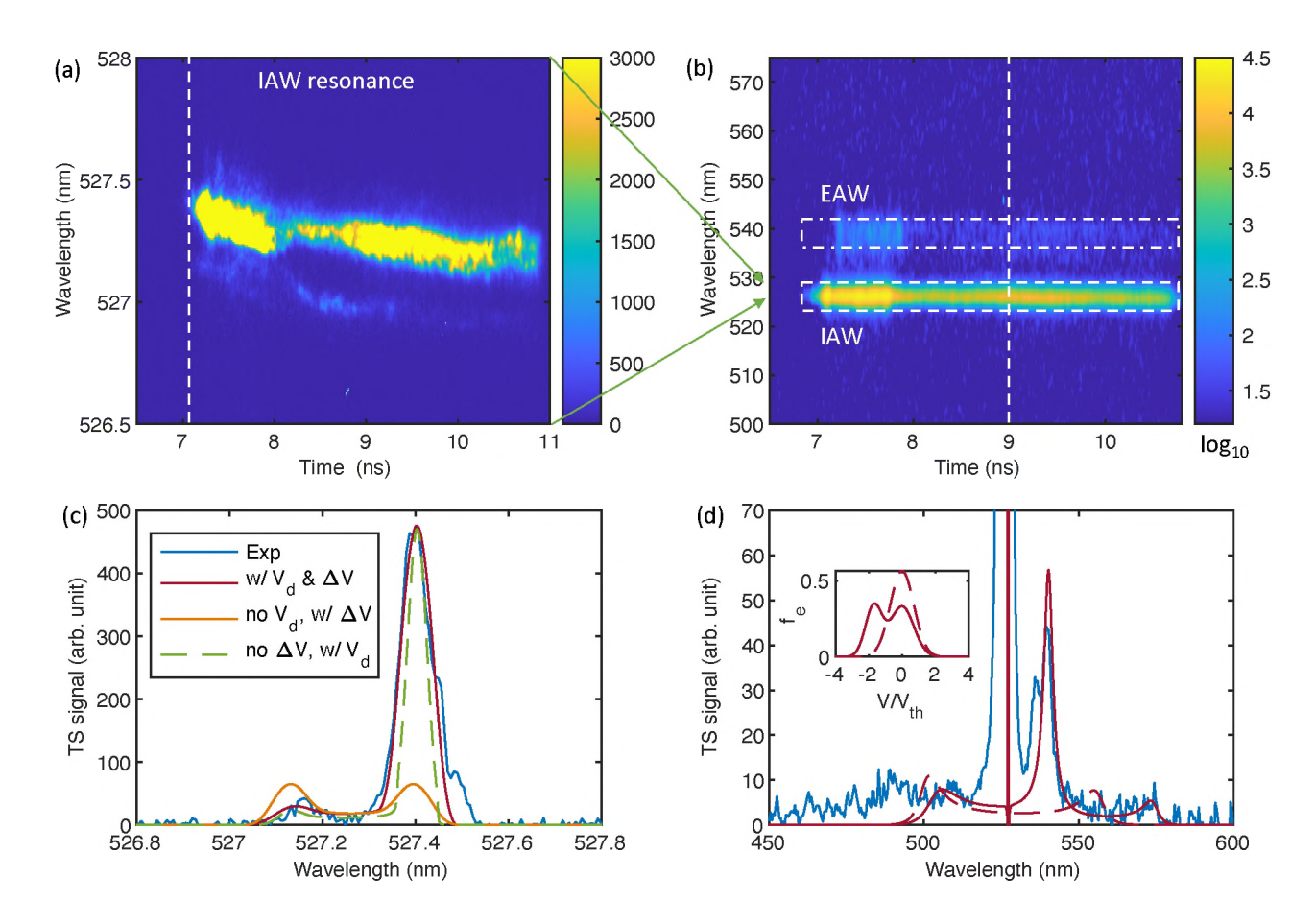


FIG. 2. (a) (b) Time-resolved Thomson scattering (TS) at t=7-10 ns. The IAW resonant peaks in (a) are highly asymmetric (grow from 10:1 to 100:1). The spectrum at 7.1 ns, before the IAW bursts, along the vertical dashed line in (a) is plotted in (c) as the blue line and compared with the synthetic TS spectra. The green dashed synthetic spectrum in (c) can reproduce the asymmetry of the IAW peaks, which is calculated with electrons streaming relative to ions with  $v_d = 0.17v_{\rm th}$  along the k-direction (red arrow) in Fig. 1b. In addition to the electron drift, an inhomogeneous flow velocity with  $\Delta v = 2 \times 10^4$  m/s~  $v_i$  in the scattering volume can broaden the IAW peak, shown as the red solid line, to match the experiment. A plasma without a drift but with an inhomogeneous flow velocity would generate a symmetric IAW spectrum, shown as the orange line. (b) is the spectrogram from the broadband spectrometer showing both the EAW resonance and the IAW feature. The spectrum at 9 ns (along vertical dashed line of (b)) is plotted in (d) with a fitted synthetic spectrum (red solid line). A two-stream electron distribution, shown as the solid line in the inserted plot, is needed to reproduce the strong EAW signal. -v direction is along the redshifted k in Fig. 1b. The velocity at the valley of the distribution (-0.023c) matches the EAW's phase velocity (0.025c). For reference, a Maxwellian distribution, shown as the dashed line in the inserted figure, would generate the dashed spectrum.

persion equation,

$$\begin{split} 1 - \frac{\omega_{\mathrm{pe}}^2}{2k^2 T_{\mathrm{e}}/m_{\mathrm{e}}} \mathbf{Z}' \left( \frac{\omega/k - v_{\mathrm{d}}}{\sqrt{2T_{\mathrm{e}}/m_{\mathrm{e}}}} \right) \\ - \frac{\omega_{\mathrm{pi}}^2}{2k^2 T_{\mathrm{i}}/m_{\mathrm{i}}} \mathbf{Z}' \left( \frac{\omega/k}{\sqrt{2T_{\mathrm{i}}/m_{\mathrm{i}}}} \right) = 0, \quad (1) \end{split}$$

where Z' is the derivative of the plasma dispersion function [45], the plasma with this strong electron drift is unstable to IAW, and the maximum growth rate is  $17 \text{ ns}^{-1} (1.4 \times 10^{-4} \omega_{\text{pe}})$ , and 0.058 ns e-folding time) at  $k = 0.33/\lambda_{\text{D}}$ . This IAW growth agrees with exponential growth of the scattering signal, which is proportional

to the square of the density fluctuation. As shown in Fig. 3(b), before the first spike, the TS IAW signal exponentially grows with an 0.025 ns e-folding time, about 40% of the calculated IAW growth rate. The intensity of the IAW scattering is 3 orders higher than that when no burst presents near 5 ns, indicating that the fluctuation amplitude  $(\delta n/n$  at  $k=2\pi/527$  nm<sup>-1</sup>) is ~30 times higher than the thermal level.

With about 0.12 ns delay from the bursts of the IAW (see Fig. 3(c)), the EAW appears with spectra red-shifted by  $\sim$ 13 nm wavelength, corresponding to a phase velocity of  $0.025c \sim 1.2 \sqrt{T_{\rm e}/m_{\rm e}}$ . This EAW peak can be reproduced with a two-stream distribution shown in Fig. 2(d). The red solid line in the inserted figure is the two-stream

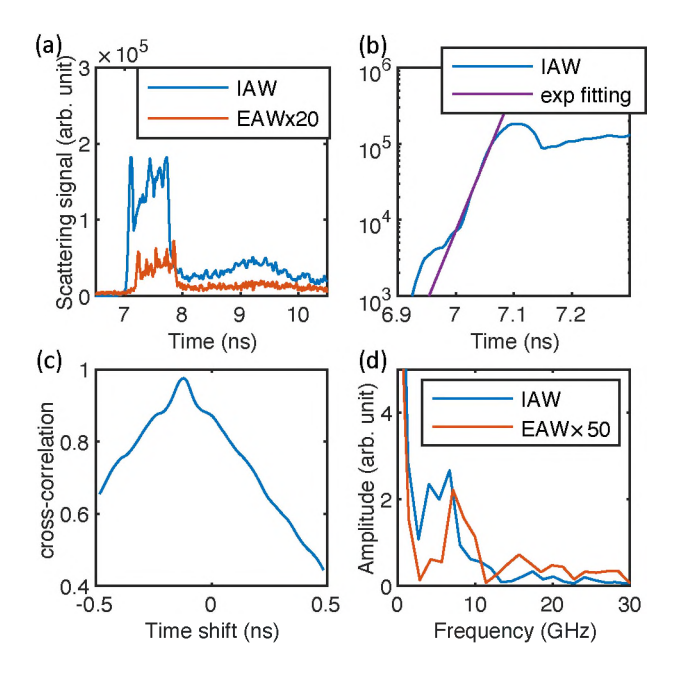


FIG. 3. (a) IAW and EAW Thomson scattering signal in the dash-boxed (IAW) dash-dot-boxed (EAW) region shown in Fig. 2(b). Bursts of IAW and EAW are shown around 7 – 8 ns. (b) IAW signal before the first burst fitted by an exponential function with e-folding time 0.025 ns (3200  $w_{\rm pe}^{-1}$ ), agreeing with the IAW growth rate,  $\gamma \sim 1.4 \times 10^{-4} w_{\rm pe}$ . (c) Cross-correlation of the IAW and EAW signal shows a strong correlation between IAW and EAW. IAW is leading EAW by 0.12 ns  $\sim 1.5 \times 10^4 \omega_{\rm pe}^{-1}$ . (d) The Fourier transform of the 7–8 ns signal shows that both IAW and EAW signals are oscillating with an amplitude peak frequency at 7 GHz. This frequency matches the lower-hybrid frequency in a 20 T magnetic field.

distribution that produces the synthetic spectrum with a strong EAW peak (red solid line). The velocity at the valley of the distribution matches the phase velocity of the EAW peak.

The amplitude of IAW and EAW during the bursty period (7–8 ns) is shown to be modulated at a frequency of  $\sim$ 7 GHz (Fig. 3d), close to the the lower-hybrid frequency  $(\sqrt{f_{ce}f_{ci}})$  at B=20 T. One candidate to explain such observations is the Modified Two-Stream Instability (MTSI) [24] driven by the electron outflow jet perpendicular to the local magnetic field in the exhaust region. The MTSI can generate electric field fluctuations nearly parallel to the current, which may modulate the IAW and the generation of EAW bursts. Waves near the lower-hybrid frequency were often observed in the MMS (Magnetospheric Multi-Scale) mission [e.g. 46] and the MRX (Magnetic Reconnection Experiment) [e.g. 16] and have been suggested to mediate energy dissipation. This modulation near the lower-hybrid frequency suggests the instabilities like MTSI may affect the electron outflow but further study is needed to characterize the role of this lower-hybrid modulation.

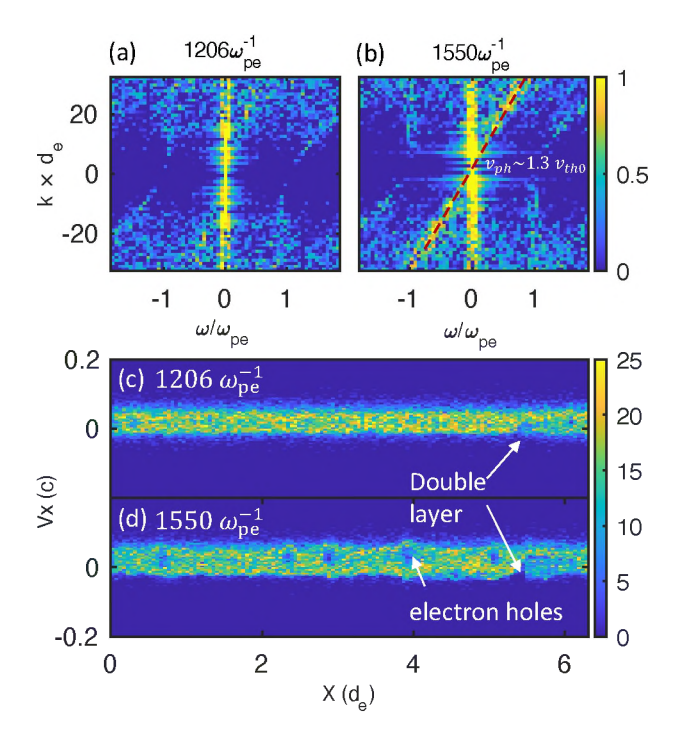


FIG. 4. (a) and (b) Electron density dispersion plots before  $(t=1206\omega_{\rm pe}^{-1})$  and during the EAW bursts  $(t=1550\omega_{\rm pe}^{-1})$ . The red dashed line is the dispersion relation with  $v_{\rm ph}=1.3\sqrt{T_{\rm e}/m_{\rm e}}$ . (c) and (d) are the electron phase spaces at the times of (a) and (b). (c) shows the double layer starts to form at  $t=1206\omega_{\rm pe}^{-1}$ . (d) After forming the double layer at  $t=1550\omega_{\rm pe}^{-1}$ , the electrons holes are generated due to the two-stream instabilities. These electron holes are moving in the +x direction with a velocity of  $1.3\sqrt{T_{\rm e}/m_{\rm e}}$ , forming the EAW bursts shown in (b).

Electron heating is also captured since electron temperature increases by 60% during the bursts of IAW and EAW. Electron temperature is measured from the separation between the IAW's Stokes and anti-Stokes peaks, which is proportional to the ion-acoustic velocity as  $\Delta\omega \sim 2k\sqrt{ZT_{\rm e}/m_{\rm i}}$ . This IAW peak separation increases by 25% before (7.0 ns) and after (8.5 ns) the IAW and EAW bursts.

#### 1D LOCAL PARTICLE-IN-CELL SIMULATION

To understand the bursts of the correlated IAW and EAW, we have used a 1D electrostatic particle-in-cell code [47] to simulate the thermal electrons (initial electron temperature  $T_{\rm e0}=320$  eV) drifting relative to ions with a velocity  $v_{\rm d}=0.5\sqrt{T_{\rm e0}/m_{\rm e}}$ .

The bursts of IAW and EAW are reproduced in the 1D PIC simulation, as shown in Fig. 4. The dispersion plot Fig. 4(b) shows that the EAW burst has a phase velocity of  $\sim 1.3 \sqrt{T_{\rm e0}/m_{\rm e}}$  with a broadband frequency of  $\sim (0.1-1)~\omega_{\rm pe}$ . This phase velocity roughly agrees

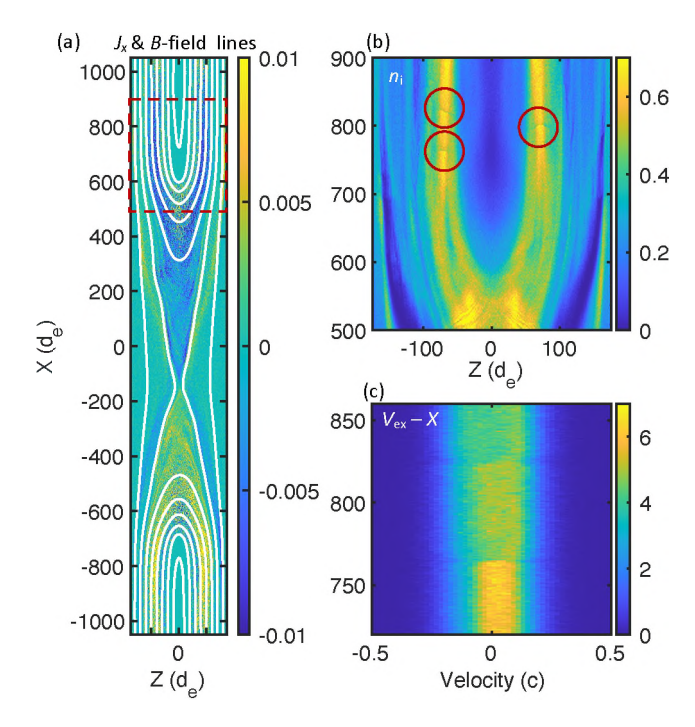


FIG. 5. Results of the 2D reconnection PIC simulation with  $m_{\rm i}/m_{\rm e}=1600$  at  $10400~\omega_{\rm pe}^{-1}$ . (a) The entire profile of the background electron current in x-direction  $(J_x=en_{\rm e,bg}v_x)$  with magnetic field lines. (b) A cropped region of the background plasma's ion density in the outflow region (red dashes in a). The double layers, shown as the ion cavities, are cycled in red. (c) Electron phase space profile along  $z=-74d_{\rm e}$  crossing the double layers at x=765 and  $825~d_{\rm e}$ .

with the experimentally observed EAW's phase velocity  $\sim 1.2\sqrt{T_{\rm e}/m_{\rm e}}$ . In the phase space shown in Fig. 4(d), this EAW corresponds to the phase space holes originated from the electron-two-stream instability in the downstream of a double layer generated by the unstable IAW. This double layer reflects low-energy electrons and accelerates high-energy electrons that can overcome the potential well, resulting in a two-stream distribution. This process has been discovered in Vlasov simulations [48], which also shows that, with realistic mass ratio, the double layer occurs  $\sim 10^4 \omega_{\rm pe}^{-1}$  after the peak of the IAW fluctuations, which is consistent with the observed 0.12 ns  $\sim 1.5 \times 10^4 \omega_{\rm pe}^{-1}$  delay between the EAW and IAW bursts.

#### 2D GLOBAL PARTICLE-IN-CELL SIMULATION

In addition to the 1D local PIC simulation showing the unstable IAW-generated double layer and EAWs, our 2D PIC reconnection simulation also confirms the double layer generation in the outflow region when cold background plasma is present. In the 2D reconnection simulation with cold background plasma, double layers in the outflow are developed and create non-Maxwellian and

broadened distributions in the double layer downstream. Figure 5(a) is the in-plane current map and magnetic field lines in the entire simulation domain. The ion density profile in the outflow region is shown in Fig. 5(b), in which the double layers are presented as the ion cavities cycled in red. The electron phase space profile crossing the double layers at  $z=-74d_{\rm e}$  is plotted in Fig. 5(c). As shown in the phase space profile, upstream of the double layers, the electrons are drifting relative to ions, which can destabilize IAW forming double lay-In the downstream, the distribution is broadened and shows a non-Maxwellian distribution with double peaks. Besides the current-driven unstable IAW, ionion acoustic instability [49] is also shown in the region with two-streaming ions ( $x \sim 500 d_{\rm e}$  in Fig. 5b), especially in the 100 and 400 mass ratio cases. However, this ion-ion acoustic instability only creates strong density perturbations; no non-Maxwellian distribution is seen in electron phase space. In the meanwhile, the double layers and the non-Maxwellian distribution in the downstream are persistent with different mass ratios. The observation of the current-driven double layers and the induced non-Maxwellian distribution confirm that, with cold background plasmas, the current-driven IAW bursts can result in energy dissipation in the outflow region.

#### DISCUSSION AND OUTLOOK

In summary, our low- $\beta$  magnetic reconnection experiments using laser-driven capacitor coils exhibit current-driven IAW bursts, followed by EAW bursts with electron heating in the exhaust region.

The location and wave direction are consistent with the IAWs observed by MMS [50], THEMIS (Time History of Events and Macroscale Interactions during Substorms) [51], and PSP (Parker Solar Probe) [52] when a population of cold ions exist in the background and their Landau damping is ineffective. These observations suggest that the current-driven instabilities can lead to a bursty magnetic field energy release. As our 1D and 2D PIC simulations reveal, this energy dissipation process involves IAW-formed double layers producing two-streaming electrons downstream, which induces the electron two-stream instability. This rapidly heats the electrons, braking the electron outflow jet. Such a double-layer-induced electron two-stream instability may also explain the origin of the EAWs observed by MMS [53].

This dissipation process in the reconnection exhaust region is confirmed in our experiment; whether this process can occur in the current sheet region needs further study. A similar mechanism has been observed in the current sheet of a 3D PIC simulation with a strong guide field, in which Buneman instability [12] leads to a formation of double layers and triggers electron two-stream instability [14]. In 1D simulations, the Buneman-instability-

generated double layer also creates ion and electron phase space holes [54, 55]. However, without a guide field or with a weak guide field, the electrons would be deflected out of the current sheet within a short period, which is shown in 3D simulations with a finite guide field [56]. The non-steady electron stream in the current sheet may interrupt the instabilities' growth. The growth of IAW and double layer needs  $\sim 10^3 - 10^4 \omega_{\rm pe}^{-1}$ , as suggested by our experiment. In addition to the time needed, Vlasov simulation and previous particle simulations [57] all demonstrate that generating the double layer requires a large system size (>  $500\lambda_{\rm De}$ ). Future experiments and large-scale 3D simulations are needed to study the current sheet region.

The IAW-type turbulence may be important for stellar flares and other plasmas where magnetic reconnection is prevalent, including those of black hole accretion engines. During the initial transient phase of stellar flares, electrons are heated to high temperatures, and ions could remain cold and evade detection [58]. This condition favors destabilizing IAWs to dissipate current and thus magnetic free energy via electrostatic double layers, in turn triggering EAW and further heating electrons. Type-III and type-U radio emission [59] could be generated by electron beams out of double layer structures. Other two-temperature plasmas, in which the electrons may be much cooler than ions, may exist in strongly magnetized black hole accretion disk corona [60] or regions within collisionless accretion flows [61, 62]. Here, the relative drift between electrons and ions can be sufficiently large compared with the electron thermal speed to overcome ion Landau damping due to simultaneous low density and low electron temperature (or equivalently electron  $\beta \ll 1$ ), and thus unstable IAW or the related Buneman instabilities may be viable mechanisms to efficiently dissipate magnetic energy.

S. Z. would like to thank Dr. Qing Wang for fruitful discussions. We acknowledge the OMEGA laser facility staff at the Laboratory for Laser Energetics. The experiment was conducted at the Omega Laser Facility with the beam time through the National Laser Users' Facility (NLUF) (or the Laboratory Basic Science) under the auspices of the U.S. DOE/NNSA by the University of Rochester's Laboratory for Laser Energetics under Contract DE-NA0003856, and the DOE Office of Science under the HEDLP program with award number DE-SC0020103. The FLASH code used in this work was in part developed by the DOE NNSA-ASC OASCR Flash Center at the University of Chicago. The authors would like to acknowledge the OSIRIS Consortium, consisting of UCLA and IST (Lisbon, Portugal) for providing access to the OSIRIS 4.0 framework supported by NSF ACI-1339893.

#### **METHODS**

In the methods section we present the setup of the Thomson scattering diagnostics, the calculation of the synthetic Thomson scattering spectrum and the parameters of the 1D and 2D PIC simulations. The FLASH radiative-non-ideal magnetohydrodynamic simulations and the proton radiography used to confirm the existence of reconnection are presented in the supplemental materiel.

#### Collective Thomson scattering

In this experiment, a f/10 reflective collection system  $60^{\circ}$  off the probe's axis [63] collects the Thomson scattering of the probe light from a  $60\times60\times50~\mu\text{m}^3$  volume near the focus. A narrowband (7 nm window) and a broadband (320 nm window) streaked spectrometers temporally and spectrally resolved the collected scattering light. The streak window is 5 ns. The narrowband spectrometer covers the light scattered by ion-acoustic waves. The spectrometer spectrometer can show the spectrum peaks scattered by ion-acoustic waves, electron-acoustic waves, and electron plasma waves. The timing of the probe is changed for each shot to cover the entire reconnection process.

To forward fit the measured Thomson scattering spectrum, we calculated synthetic power spectrum in Fig. 6 and Fig. 2 based on the model which has also been used in Ref. [64, 65]. The synthetic power spectrum is

$$P(\lambda_s) \propto \left(1 + \frac{2\omega}{\omega_0}\right) \left[\frac{2\pi}{k} \left| \frac{1 + \chi_i}{1 + \chi_e + \chi_i} \right|^2 f_e\left(\frac{\omega}{k}\right) + \frac{2\pi Z}{k} \left| \frac{\chi_e}{1 + \chi_e + \chi_i} \right|^2 f_i\left(\frac{\omega}{k}\right) \right] \frac{d\omega}{d\lambda_s}, \quad (2)$$

where  $\omega = \omega_0 - \omega_s$  is the angular frequency of the fluctuations scattering the probe light  $(\omega_0, \mathbf{k}_0)$  and generating the scattered light  $(\omega_s, \mathbf{k}_s)$ , and  $f_{e,i}(v)$  are the electron/ion velocity distributions reduced to 1D along  $\mathbf{k}$  direction. The electron and ion susceptibilities are given by

$$\chi_{\rm e,i}(\omega,k) = \int_{-\infty}^{\infty} dv \frac{\omega_{\rm pe,i}^2}{k^2} \frac{k \partial f_{\rm e,i} / \partial v}{\omega - kv}.$$
 (3)

## Electron acoustic wave resonance in Thomson scattering

Figure 6(a) shows the time evolution of the Thomson scattering spectrum from the broadband spectrometer, and the spectrum at 2.9 ns is shown as the blue line in Fig. 6(b). In addition to the resonant peaks scattered

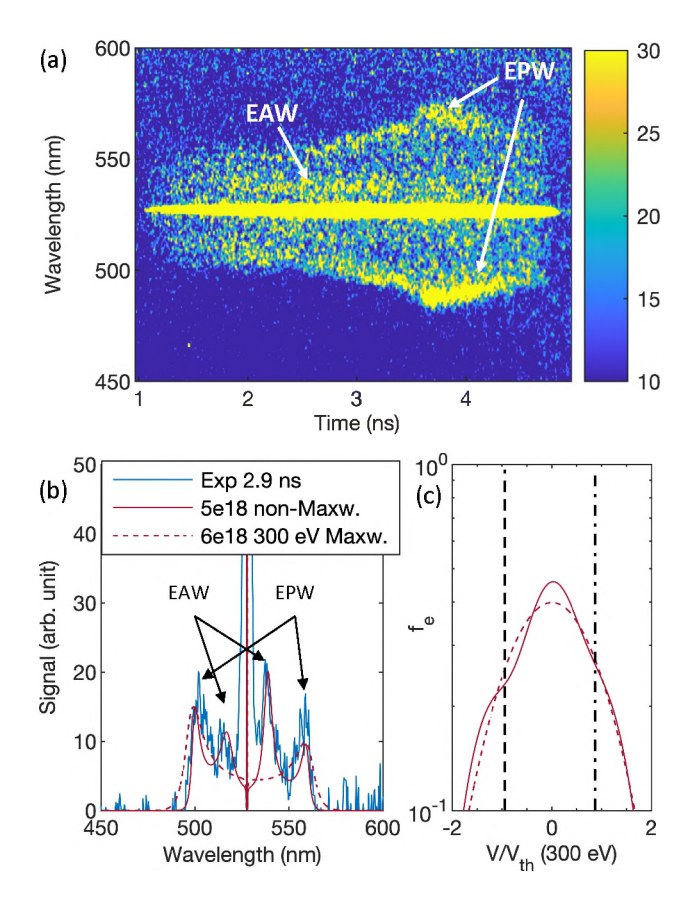


FIG. 6. (a) Time-resolved Thomson scattering (TS) shows features of electron plasma waves (EPW) and electron acoustic waves (EAW). The UV lasers onset at 0 ns. (b) Comparison between the measured TS spectrum at t=2.9 ns and the synthetic TS spectra with Maxwellian electrons ( $T_{\rm e}=300~{\rm eV},$  dashed) vs. non-Maxwellian electrons (solid). The velocity distribution functions are plotted in (c). The non-Maxwellian distribution (solid line in c) is constructed with two secondary components ( $n_{\rm e}=1.15\times10^{18}~{\rm cm}^{-3},\,T_{\rm e}=75~{\rm eV})$  streaming with  $-1.2v_{\rm th,300eV}$  and  $+1.1v_{\rm th,300eV}$  relative to a steady electron component ( $n_{\rm e}=2.7\times10^{18}~{\rm cm}^{-3},\,T_{\rm e}=75~{\rm eV}).$  -v direction is along the redshifted k in Fig. 1b. This non-Maxwellian distribution reduced the slope near the phase velocities of the EAWs, marked with a dashed line corresponding to the EAW at 539 nm and a dash-dotted line for the EAW at 517 nm. The non-Maxwellian component is required to match the data.

by electron plasma waves (EPW) usually seen in laser plasma experiments, the Thomson scattering spectrum also shows resonant peaks with lower wavelength shift (~10 nm) indicating the non-Maxwellian distribution in the reconnection exhaust. These shorter wavelength resonant peaks are caused by EAWs with phase velocities near the electron thermal velocity  $v_{\rm e,th} = \sqrt{T_{\rm e}/m_{\rm e}}$ , which would be Landau damped if the electron velocity distribution were Maxwellian, as shown in the red dashed line in Fig. 6(b). To reproduce the EAW peaks, we modified the distribution function by combining two counter-streaming beams with the steady component to

reduce the slope near the thermal speed shown as the red solid line in Fig. 6(c). The corresponding synthetic scattering spectrum is calculated following Ref. [65], which is shown as the red solid line in Fig. 6(b), matches the measured spectrum. This three-component velocity distribution is similar to the observed ring-core distribution in 2D PIC simulations of reconnection [66], in which the ring in the outflow-out-of-plane phase space  $(v_x - v_y)$  reduces to two counter-streaming beams in  $v_x$ . This ring structure is likely produced by the reconnected magnetic field  $(B_y)$  turning the accelerated electrons [67]. Similar ring-core distribution has also been observed by MMS in the reconnection exhaust region [5, 6].

#### 1D PIC simulation

The simulation was performed in a  $2\pi c/\omega_{\rm pe}$  periodic domain with a reduced ion mass  $m_{\rm i}/m_{\rm e}=100$  and a lower ion temperature  $T_{\rm i}=20$  eV to keep the ion thermal speed lower than the IAW's phase velocity. The simulation domain contains 256 cells and 128 particles per cell. To mimic the induction electric field that would arise from the dissipation of the bipolar magnetic field, we have added an external electric field  $E_x=10^{-5}m_{\rm e}c\omega_{\rm pe}/e$  to the electric field calculated by the Poisson equation for advancing the particles' velocity.

#### 2D PIC simulation

The 2D PIC simulations use OSIRIS code [68, 69] with Harris current sheet [70] and a cold background plasma with density profile as

$$n_{\rm bg}(z) = 0.3 n_0 \left[ \frac{1}{2} + \frac{1}{2} \tanh\left(\frac{|z| - 2L}{0.5L}\right) \right],$$
 (4)

where  $n_0$  is the peak density of the Harris current sheet and  $L=20d_{\rm e}$ . This simulation setup is similar to the cold background simulation described in Ref. [71]. The Harris current sheet has hot ions with  $T_{\rm i,harris}=5T_{\rm e,harris}$ . The background plasma is initialized with  $T_{\rm i,bg}=T_{\rm e,bg}=T_{\rm e,harris}/25$ . The simulation has a  $2100d_{\rm e}\times350d_{\rm e}$  box size in  $6144\times1024$  cells. The boundaries are periodic in x direction. The z direction boundaries are reflective for particles and conductive for electric field. The anti-parallel magnetic field is in x direction with  $B_x=B_0 \tanh(z/L)$ , where  $L=20d_{\rm e}$  and  $B_0/em_{\rm e}=\omega_{\rm ce}=0.5\omega_{\rm pe}$ . The mass ratio was scanned with  $m_{\rm i}/m_{\rm e}=100,400$  and 1600. A long-wavelength perturbation [72] with  $0.01B_0$  amplitude is included to initialize reconnection.

shuzhang@princeton.edu

- † hji@pppl.gov
- M. Yamada, R. Kulsrud, and H. Ji, Rev. Mod. Phys. 82, 603 (2010).
- [2] H. Ji, W. Daughton, J. Jara-Almonte, A. Le, A. Stanier, and J. Yoo, Nat. Rev. Phys. 4 (2022), 10.1038/s42254-021-00419-x.
- [3] M. Hesse, K. Schindler, J. Birn, and M. Kuznetsova, Phys. Plasmas 6, 1781 (1999).
- [4] R. Kulsrud, H. Ji, W. Fox, and M. Yamada, Phys. Plasmas 12, 082301 (2005).
- [5] J. L. Burch, R. B. Torbert, T. D. Phan, L.-J. Chen, T. E. Moore, R. E. Ergun, J. P. Eastwood, D. J. Gershman, P. A. Cassak, M. R. Argall, S. Wang, M. Hesse, C. J. Pollock, B. L. Giles, R. Nakamura, B. H. Mauk, S. A. Fuselier, C. T. Russell, R. J. Strangeway, J. F. Drake, M. A. Shay, Y. V. Khotyaintsev, P.-A. Lindqvist, G. Marklund, F. D. Wilder, D. T. Young, K. Torkar, J. Goldstein, J. C. Dorelli, L. A. Avanov, M. Oka, D. N. Baker, A. N. Jaynes, K. A. Goodrich, I. J. Cohen, D. L. Turner, J. F. Fennell, J. B. Blake, J. Clemmons, M. Goldman, D. Newman, S. M. Petrinec, K. J. Trattner, B. Lavraud, P. H. Reiff, W. Baumjohann, W. Magnes, M. Steller, W. Lewis, Y. Saito, V. Coffey, and M. Chandler, Science 352, aaf2939 (2016).
- [6] R. B. Torbert, J. L. Burch, T. D. Phan, M. Hesse, M. R. Argall, J. Shuster, R. E. Ergun, L. Alm, R. Nakamura, K. J. Genestreti, D. J. Gershman, W. R. Paterson, D. L. Turner, I. Cohen, B. L. Giles, C. J. Pollock, S. Wang, L.-J. Chen, J. E. Stawarz, J. P. Eastwood, K. J. Hwang, C. Farrugia, I. Dors, H. Vaith, C. Mouikis, A. Ardakani, B. H. Mauk, S. A. Fuselier, C. T. Russell, R. J. Strangeway, T. E. Moore, J. F. Drake, M. A. Shay, Y. V. Khotyaintsev, P.-A. Lindqvist, W. Baumjohann, F. D. Wilder, N. Ahmadi, J. C. Dorelli, L. A. Avanov, M. Oka, D. N. Baker, J. F. Fennell, J. B. Blake, A. N. Jaynes, O. Le Contel, S. M. Petrinec, B. Lavraud, and Y. Saito, Science 362, 1391 (2018).
- [7] H. Ji, Y. Ren, M. Yamada, S. Dorfman, W. Daughton, and S. P. Gerhardt, Geophys. Res. Lett. 35, L13106 (2008).
- [8] G. Cozzani, Y. V. Khotyaintsev, D. B. Graham, J. Egedal, M. André, A. Vaivads, A. Alexandrova, O. Le Contel, R. Nakamura, S. A. Fuselier, C. T. Russell, and J. L. Burch, Phys. Rev. Lett. 127, 215101 (2021), arXiv:2103.12527 [physics.plasm-ph].
- [9] G. Lapenta, S. Markidis, A. Divin, D. Newman, and M. Goldman, Journal of Plasma Physics 81, 325810109 (2015).
- [10] C. Kennel and H. Petschek, J. Geophys. Res. 71, 1 (1966).
- [11] M. V. Goldman, D. L. Newman, G. Lapenta, L. Andersson, J. T. Gosling, S. Eriksson, S. Markidis, J. P. Eastwood, and R. Ergun, Phys. Rev. Lett. 112, 145002 (2014).
- [12] O. Buneman, Phys. Rev. Lett. 1, 8 (1958).
- [13] J. Drake, M. Swisdak, C. Cattell, M. Shay, B. Rogers, and A. Zeiler, Science 299, 873 (2003).
- [14] H. Che, J. F. Drake, M. Swisdak, and P. H. Yoon, Phys. Rev. Lett. 102, 145004 (2009).
- [15] T. Carter, H. Ji, F. Trintchouk, M. Yamada, and R. Kulsrud, Phys. Rev. Lett. 88, 015001 (2002).
- [16] H. Ji, S. Terry, M. Yamada, R. Kulsrud, A. Kuritsyn, and Y. Ren, Phys. Rev. Lett. 92, 115001 (2004).

- [17] H. Ji, R. Kulsrud, W. Fox, and M. Yamada, J. Geophys. Res. 110, A08212 (2005).
- [18] W. Fox, M. Porkolab, J. Egedal, N. Katz, and A. Le, Phys. Plasmas 17, 072303 (2010).
- [19] J. Yoo, J. Jara-Almonte, E. Yerger, S. Wang, T. Qian, A. Le, H. Ji, M. Yamada, W. Fox, E.-H. Kim, et al., Geophysical Research Letters 45, 8054 (2018).
- [20] D. B. Graham, Y. V. Khotyaintsev, C. Norgren, A. Vaivads, M. André, J. Drake, J. Egedal, M. Zhou, O. Le Contel, J. Webster, et al., Journal of Geophysical Research: Space Physics 124, 8727 (2019).
- [21] L.-J. Chen, S. Wang, O. Le Contel, A. Rager, M. Hesse, J. Drake, J. Dorelli, J. Ng, N. Bessho, D. Graham, L. B. Wilson, T. Moore, B. Giles, W. Paterson, B. Lavraud, K. Genestreti, R. Nakamura, Y. V. Khotyaintsev, R. E. Ergun, R. B. Torbert, J. Burch, C. Pollock, C. T. Russell, P.-A. Lindqvist, and L. Avanov, Phys. Rev. Lett. 125, 025103 (2020).
- [22] J. Yoo, J.-Y. Ji, M. V. Ambat, S. Wang, H. Ji, J. Lo, B. Li, Y. Ren, J. Jara-Almonte, L.-J. Chen, et al., Geophysical Research Letters 47, e2020GL087192 (2020).
- [23] N. Krall and P. Liewer, Phys. Rev. A 4, 2094 (1971).
- [24] J. McBride, E. Ott, J. Boris, and J. Orens, Phys. Fluids 15, 2367 (1972).
- [25] W. Daughton, J. Geophys. Res. 104, 28701 (1999).
- [26] T. Nakamura, H. Hasegawa, W. Daughton, S. Eriksson, W. Y. Li, and R. Nakamura, Nature communications 8, 1 (2017).
- [27] B. Coppi and A. B. Friedland, The Astrophysical Journal 169, 379 (1971).
- [28] D. F. Smith and E. Priest, The Astrophysical Journal 176, 487 (1972).
- [29] F. Coroniti and A. Evitar, Ap. J. Suppl. Series 33, 89 (1977).
- [30] R. Z. Sagdeev, Rev. Mod. Phys. **51**, 1 (1979).
- [31] M. Ugai and T. Tsuda, J. Plasma Phys. 17, 337 (1977).
- [32] T. Sato and T. Hayashi, Phys. Fluids 22, 1189 (1979).
- [33] J. Aparicio, M. G. Haines, R. J. Hastie, and J. P. Wainwright, Physics of Plasmas 5, 3180 (1998), https://doi.org/10.1063/1.873046.
- [34] R. Kulsrud, Phys. Plasmas 5, 1599 (1998).
- [35] R. Kulsrud, Earth Planets Space 53, 417 (2001).
- [36] D. A. Uzdensky, Astrophys. J. **587**, 450 (2003).
- [37] W. Gekelman and R. Stenzel, Journal of Geophysical Research: Space Physics 89, 2715 (1984).
- [38] A. Chien, L. Gao, S. Zhang, H. Ji, E. G. Blackman, W. Daughton, A. Stanier, A. Le, F. Guo, R. Follett, H. Chen, G. Fiksel, G. Bleotu, R. C. Cauble, S. N. Chen, A. Fazzini, K. Flippo, O. French, D. H. Froula, J. Fuchs, S. Fujioka, K. Hill, S. Klein, C. Kuranz, P. Nilson, A. Rasmus, and R. Takizawa, "Direct measurement of non-thermal electron acceleration from magnetically driven reconnection in a laboratory plasma," (2022), arXiv:2201.10052 [physics.plasm-ph].
- [39] T. Boehly, D. Brown, R. Craxton, R. Keck, J. Knauer, J. Kelly, T. Kessler, S. Kumpan, S. Loucks, S. Letzring, F. Marshall, R. McCrory, S. Morse, W. Seka, J. Soures, and C. Verdon, Optics Communications 133, 495 (1997).
- [40] L. Gao, H. Ji, G. Fiksel, W. Fox, M. Evans, and N. Alfonso, Physics of Plasmas 23, 043106 (2016), https://doi.org/10.1063/1.4945643.
- [41] A. Chien, L. Gao, H. Ji, X. Yuan, E. G. Blackman, H. Chen, P. C. Efthimion, G. Fiksel, D. H. Froula, K. W. Hill, K. Huang, Q. Lu, J. D. Moody, and

- P. M. Nilson, Physics of Plasmas **26**, 062113 (2019), https://doi.org/10.1063/1.5095960.
- [42] A. Chien, L. Gao, S. Zhang, H. Ji, E. Blackman, H. Chen, G. Fiksel, K. Hill, and P. Nilson, Physics of Plasmas 28, 052105 (2021), https://doi.org/10.1063/5.0044048.
- [43] B. Fryxell, K. Olson, P. Ricker, F. X. Timmes, M. Zingale, D. Q. Lamb, P. MacNeice, R. Rosner, J. W. Truran, and H. Tufo, The Astrophysical Journal Supplement Series 131, 273 (2000).
- [44] C. C. Daughney, L. S. Holmes, and J. W. M. Paul, Physical Review Letters 25, 497 (1970).
- [45] B. D. Fried and S. D. Conte, The plasma dispersion function: the Hilbert transform of the Gaussian (Academic Press, 1961).
- [46] Y. V. Khotyaintsev, D. B. Graham, K. Steinvall, L. Alm, A. Vaivads, A. Johlander, C. Norgren, W. Li, A. Divin, H. S. Fu, K.-J. Hwang, J. L. Burch, N. Ahmadi, O. Le Contel, D. J. Gershman, C. T. Russell, and R. B. Torbert, Phys. Rev. Lett. 124, 045101 (2020).
- [47] G. Lapenta, "Particle in cell methods with application to simulations in space weather," .
- [48] A. R. Vazsonyi, K. Hara, and I. D. Boyd, Physics of Plasmas 27, 112303 (2020), https://doi.org/10.1063/5.0019729.
- [49] S. P. Gary and N. Omidi, Journal of Plasma Physics 37, 45–61 (1987).
- [50] K. Steinvall, Y. V. Khotyaintsev, D. B. Graham, A. Vaivads, M. André, and C. T. Russell, Geophysical Research Letters 48, e2020GL090286 (2021).
- [51] H. Uchino, S. Kurita, Y. Harada, S. Machida, and V. Angelopoulos, Journal of Geophysical Research: Space Physics 122, 3291 (2017).
- [52] F. S. Mozer, C. A. Cattell, J. Halekas, I. Y. Vasko, J. L. Verniero, and P. J. Kellogg, "Core electron heating by triggered ion acoustic waves in the solar wind," (2021), arXiv:2111.07161 [astro-ph.SR].
- [53] R. E. Ergun, J. C. Holmes, K. A. Goodrich, F. D. Wilder, J. E. Stawarz, S. Eriksson, D. L. Newman, S. J. Schwartz, M. V. Goldman, A. P. Sturner, D. M. Malaspina, M. E. Usanova, R. B. Torbert, M. Argall, P.-A. Lindqvist, Y. Khotyaintsev, J. L. Burch, R. J. Strangeway, C. T. Russell, C. J. Pollock, B. L. Giles, J. J. C. Dorelli, L. Avanov, M. Hesse, L. J. Chen, B. Lavraud, O. Le Contel, A. Retino, T. D. Phan, J. P. Eastwood, M. Oieroset, J. Drake, M. A. Shay, P. A. Cassak, R. Nakamura, M. Zhou, M. Ashour-Abdalla, and M. André, Geophys. Res. Lett. 43, 5626 (2016).
- [54] R. A. Smith, Physica Scripta **T2A**, 238 (1982).
- [55] M. V. Goldman, D. L. Newman, and R. E. Ergun, Nonlinear Processes in Geophysics 10, 37 (2003).

- [56] W. Daughton, V. Roytershteyn, H. Karimabadi, L. Yin, B. Albright, B. Bergen, and K. Bowers, Nature Phys. 7, 539 (2011).
- [57] T. Sato and H. Okuda, Phys. Rev. Lett. 44, 740 (1980).
- [58] V. Polito, J. Dudík, J. Kašparová, E. Dzifčáková, K. K. Reeves, P. Testa, and B. Chen, The Astrophysical Journal 864, 63 (2018).
- [59] R. Miteva, G. Mann, C. Vocks, and H. Aurass, Astronomy & Astrophysics 461, 1127 (2007).
- [60] T. Di Matteo, E. G. Blackman, and A. C. Fabian, MN-RAS 291, L23 (1997), arXiv:astro-ph/9705079 [astro-ph].
- [61] R. Narayan, R. Mahadevan, and E. Quataert, in *Theory of Black Hole Accretion Disks*, edited by M. A. Abramowicz, G. Björnsson, and J. E. Pringle (1998) pp. 148–182.
- [62] F. Yuan and R. Narayan, Ann. Rev. Astron. Astrophys. 52, 529 (2014).
- [63] J. Katz, R. Boni, C. Sorce, R. Follett, M. J. Shoup, and D. H. Froula, Review of Scientific Instruments 83, 10E349 (2012), https://doi.org/10.1063/1.4733551.
- [64] A. L. Milder, S. T. Ivancic, J. P. Palastro, and D. H. Froula, Physics of Plasmas 26, 022711 (2019), https://doi.org/10.1063/1.5085664.
- [65] A. L. Milder, H. P. Le, M. Sherlock, P. Franke, J. Katz, S. T. Ivancic, J. L. Shaw, J. P. Palastro, A. M. Hansen, I. A. Begishev, W. Rozmus, and D. H. Froula, Physical Review Letters 124, 025001 (2020).
- [66] J. R. Shuster, L.-J. Chen, W. S. Daughton, L. C. Lee, K. H. Lee, N. Bessho, R. B. Torbert, G. Li, and M. R. Argall, Geophysical Research Letters 41, 5389 (2014).
- [67] N. Bessho, L.-J. Chen, J. R. Shuster, and S. Wang, Geophysical Research Letters 41, 8688 (2014).
- [68] R. Fonseca, L. Silva, R. Hemker, F. Tsung, V. Decyk, W. Lu, C. Ren, W. Mori, S. Deng, S. Lee, T. Katsouleas, J. Adam, and Osiris, in *Lect. Notes comput.* Sci. (Springer-Verlag, 2002) p. Vol. 2331.
- [69] R. G. Hemker, "Particle-in-cell modeling of plasmabased accelerators in two and three dimensions," (2015), arXiv:1503.00276 [physics.comp-ph].
- [70] E. Harris, Il Nuovu Cimento 23, 115 (1962).
- [71] C. Norgren, P. Tenfjord, M. Hesse, S. Toledo-Redondo, W.-Y. Li, Y. Xu, N. K. Kwagala, S. Spinnangr, H. Kolstø, and T. Moretto, Frontiers in Astronomy and Space Sciences 8, 149 (2021).
- [72] J. Birn, J. Drake, M. Shay, B. Rogers, R. Denton, M. Hesse, M. Kuznetsova, Z. Ma, A. Bhattachargee, A. Otto, and P. Pritchett, J. Geophys. Res. 106, 3715 (2001).